Rational Micro-Nano Structuring for Thin Film Evaporation

A Thesis

Presented to

The Faculty of the Department of Mechanical Engineering

University of Houston

In Partial Fulfillment

Of the Requirement for the Degree

Master of Science

In Mechanical Engineering

By

Nazanin Farokh Nia

December 2016

Rational Micro-Nano Structuring for Thin Film Evaporation

_____

Nazanin Farokh Nia

Approved:

_____
Chair of the Committee
Hadi Ghasemi, Bill D. Cook Assistant Professor,
Mechanical Engineering

Committee Members:

_____
Daniel Araya, Assistant Professor
Mechanical Engineering

_____
Haleh Ardebili, Bill D. Cook Associate Professor
Mechanical Engineering and Materials Program

_____   _____
Suresh K. Khator, Associate Dean,   Pradeep Sharma, Professor and Chair,
Cullen College of Engineering   Mechanical Engineering

Acknowledgment

Firstly, I would like to express my sincere gratitude to my advisor, Professor Hadi Ghasemi, for the continuous support of my Masters study, for his patience, motivation, and immense knowledge.

Besides my advisor, I would like to thank the rest of my thesis committee: Prof. Daniel Araya, and Prof. Haleh Ardebili.

I also take this opportunity to thank to all of my teachers specially Professor S.M.B. Malaek for their help and support during all the years of my study.

Finally, I must express my very profound gratitude to my parents, my brother, and my husband, and my friends in Nanotherm research group for providing me with unfailing support and continuous encouragement throughout my years of study and through the process of researching and writing this thesis. This accomplishment would not have been possible without them.

Rational Micro-Nano Structuring for Thin Film Evaporation

An Abstract

of a

A thesis

Presented to

The Faculty of the Department of Mechanical Engineering

University of Houston

In Partial Fulfillment

Of the Requirements for the Degree

Master of Science

In Mechanical Engineering

By

Nazanin Farokh Nia

December 2016

Abstract

Heat management in electronics and photonics devices is a critical challenge that impedes the accelerated breakthrough in these fields. Among approaches for heat dissipation, thin film evaporation with micro/nano structures has been one of the most promising approaches that can address future technological demand. The geometry and dimension of these micro/nano structures directly govern the interfacial heat flux. Here, through theoretical and experimental analysis, we find that there is an optimal dimension of micro/nano structures that maximizes the interfacial heat flux by thin film evaporation. This optimal criterion is a consequence of two opposing phenomena: non-uniform evaporation flux across a liquid meniscus (divergent mass flux near three phase contact line) and the total liquid area exposed for evaporation. This general criterion is independent of the solid material and thermo-physical properties of the cooling liquid. This study paves the path for development of high-performance thermal management systems.

Table of Contents

List of Figures

1.   Introduction

Miniaturization has been the hallmark of electronics and photonics instruments in the last few decades. The miniaturization efforts span in an enormous range of dimensions from nanoscale transistors to thumbnail-sized chips, smartphones, vehicle electronics, and server farms. This miniaturization, accompanied by enhanced functional density, necessitates enhanced heat dissipation, which has been the bottleneck of further advancement in these technologies.[1] The constantly growing CPU power density has introduced a high demand for advanced cooling systems.[2] A range of approaches has been studied to address this high heat flux challenge including jet impingement,[3] sprays,[4] and micro-channels.[5–8] However, thin film evaporation with nanometer fluid thickness is considered one of the most promising approaches to address the future demands.[9–21] In addition to the electronics/photonics cooling applications, thin film evaporation is a critical phenomenon in cooling of satellite solar arrays, shuttle reentry, HVAC systems, and medical devices.

Thin film evaporation phenomenon in micro/nano structures is a coupled multi-physics momentum transport, energy transport, and gas kinetics problem. The momentum transport governs the fluid flow to the liquid-vapor interface; the energy transport governs the heat transfer to the liquid-vapor interface, and the gas kinetics governs the evolution of molecules from liquid phase to the vapor phase at the liquid-vapor interface. All these physics are essential parts of thin film evaporation phenomenon, and the phenomenon will not proceed in absence of any of these transports. Depending on the time and length scales and the thermodynamic properties of the liquid-vapor interface,

each of these physics imposes a limit on the kinetics of thin film evaporation phenomenon. In thin film evaporation, the small fluid thickness decreases the thermal resistance between the hot solid substrate and the liquid-vapor interface, maximizing the heat flux dissipated by the solid substrate. For a given projected area of a solid, as we extend the area of thin film in a structure, the heat dissipation by the structure increases. Micro/nano structures have shown a great promise to enhance the area of thin film evaporation and consequently offer an efficient platform for heat dissipation.

Early in the development of micro/nano structures for thin film evaporation, research studies focused on transcending the momentum transport limit by development of micro/nano structures with a range of materials in various shapes. These micro/nano structures include micro-pillar arrays,[22–25] copper micro-posts,[26] sintered wick microstructures,[27] and carbon nanotubes.[28,29] In these structures, the momentum transport of fluid to the thin-film region is driven by the capillary action, resulting into coupling of capillary and viscous forces. As we move to smaller pore radius in micro/nano structures, the viscous resistance increases and eventually fluid flow will stop, thereby reaching the momentum transport limit. How- ever, development of bi-porous approach[30–39] allowed to partially raise the limit imposed by the momentum transport. In this approach, the viscous pressure of fluid flow is divided in two parts, (I) the long length of fluid flow occurs in micro-channels with small hydraulic resistance (II) the short length of fluid flow occurs in the nano-channels with high hydraulic resistance. Thus, the overall small hydraulic resistance allows raising the momentum trans- port limit and consequently boosting the interfacial heat flux by the thin-film evaporation. This bi-porous approach

partially uncouples capillary and viscous forces and allows for further development of advanced micro/nano structures for thin-film evaporation.

The geometry and dimension of the micro/nano structures have a significant role on the heat dissipation through thin film evaporation. Ranjan et al.[11,40] developed a numerical model to study the role of geometry on thin film evaporation. These authors studied four geometries of micro-structures to maximize the interfacial heat flux. These geometries include horizontal wires, rectangular ribs, vertical wires, and packed spheres. The authors concluded that the horizontal wires are performing worse than the other three geometries, which provide approximately the same interfacial heat fluxes. However, rational strategy on dimensions of these micro/nano structures remains an open question. Knowledge on these micro/nano structuring guidelines provides a path to develop micro/nano structures in a systematic approach for thin-film evaporation to address future technological demands.

Here, through detailed theoretical and experimental studies, we develop a rational direction for development of micro/nano structures for thin-film evaporation. We present optimal dimensions and arrangement of features in the micro/nano structures that maximize the interfacial heat flux. In this work, we solve Young-Laplace equation, energy equation, and Hertz-Knudsen equation at the liquid-vapor interface to determine the evaporative heat flux at the liquid-vapor interface. Through analysis of dimensional role in the micro/nano structures, we found an optimal criterion for design of micro/nano structures. To support our theoretical analysis, we fabricated microstructures and examined the thin film evaporation performance of these structures and compared the

3

results with the theoretical analysis. The goal of this work is to elucidate the general

optimal criterion for micro/nano structuring for thin film evaporation.

2. Theoretical Analysis

2.1. Model Development

Three common geometries of micro/nano structures are chosen for thin film evaporation as shown in **Fig. 1**. These model structures are the optimal configuration for thin-film evaporation as suggested by simulation of Ranjan et al.[11,63] We define width-to-spacing ratio (= w/2r). The top and side views of the studied micro/nano structures are shown in **Fig. 2**. The profile of the liquid-vapor interface and contact angle are shown by function z(y) and θ, respectively. As the pitch between the pillars is much smaller than the capillary length of the working fluid (order of mm), the gravitational force is neglected in these analyses. The meniscus profile of liquid-vapor interface, z(y), for each configuration is determined through solving the Young-Laplace equation

$$\frac{1}{R_C} = \frac{\ddot{z}(y)}{\sqrt{(1 + \dot{z}(y)^2)^3}},$$

(1)

where R_C(= r/cosθ) denotes the radius of curvature of liquid-vapor interface. The second curvature is much smaller than the first curvature and is neglected. The boundary conditions are defined as

$$z(y = 0) = -Rc * (1 - \sin\theta)$$

(2)

$$z(y = r) = 0.$$

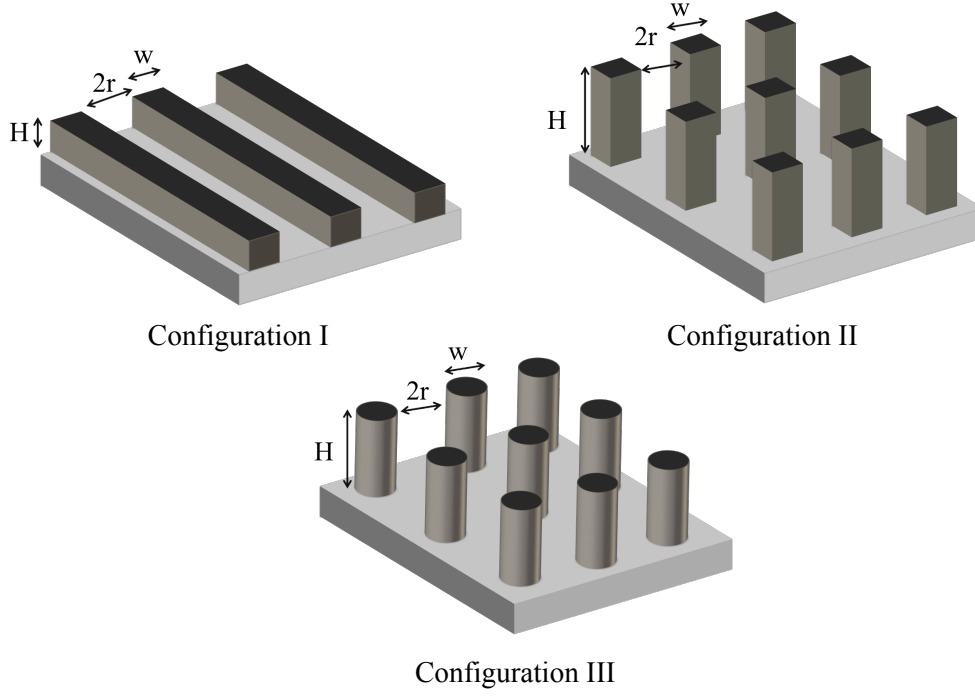| Configuration I	Configuration II

Configuration III

Figure 1. The studied model structures for thin film evaporation are shown.

The Young-Laplace equation with the given boundary conditions (r and θ) is implemented in Mathematica to determine the profile of the liquid-vapor meniscus. This approach has extensively been used to determine the profile of liquid-vapor interface.[64–67] Once the profile of liquid-vapor meniscus is determined, the evaporation flux at the liquid-vapor interface can be determined through Hertz-Knudsen equation,[68–71]

$$\dot{m} = \frac{2\sigma}{2-\sigma} \sqrt{\frac{\overline{M}}{2\pi\overline{R}}} \left(\frac{P^s(T_{lv})}{\sqrt{T_{lv}}} - \frac{P_v}{\sqrt{T_v}} \right), \tag{3}$$

where $\dot{m}$ denotes the mass flux, σ the accommodation coefficient, $\overline{M}$ the molar mass of fluid, $\overline{R}$ the molar gas constant, P^s saturation pressure of the liquid, T_{lv} liquid temperature at the interface, P_v vapor pressure at the interface, and T_v the vapor

6

temperature at the interface. The formula is derived through Kinetic Theory of Gases and there are a few assumptions involved: (1) an equilibrium exists in the Knudsen layer, (2) the mechanical equilibrium is always established at the interface during the evaporation and no spatial pressure gradient exists in the vapor phase and (3) the liquid pressure corresponds to the saturation pressure of liquid at T_{lv}. Both of assumptions (2) and (3) are justified by recent studies.[44,48,49] The accommodation coefficient is defined as the probability of crossing the interface by a molecule impinging on the surface, defined by Knudsen[50] to explain the experimental findings. The experimental measurements never showed accommodation coefficient larger than unity except in the MD simulations conducted by Holyst et al.[51] The authors argued that the Hertz-Knudsen theory is only strictly valid at equilibrium and low vapor pressure and the theory should be modified for non-equilibrium conditions. Although this coefficient seems conceptually simple, it is extremely hard to measure. Here, the accommodation coefficient of 0.3 for an evaporating water interface is considered.[52] The equilibrium condition at the Knudsen layer suggests that the vapor pressure at the interface corresponds to the saturation pressure at the vapor temperature and is determined through Clausius-Clapeyron equation similar to the liquid pressure

$$P_v = P_{ref} \exp\left(\frac{\overline{M}h_{fg}}{\overline{R}}\left(\frac{1}{T_{ref}} - \frac{1}{T_v}\right)\right), \tag{4}$$

where h_{fg} denotes the enthalpy of liquid-vapor phase change, and P_{ref} and T_{ref} correspond to the thermodynamic variables in an arbitrary reference point. Hertz-Knudsen equation, along with Eq. 4, suggests that two thermodynamic variables are

needed to determine the mass flux at the liquid-vapor interface, T_v and T_{lv}. The value of T_v is equal to T_s - ΔT, where T_s is the temperature of solid in contact with the vapor and ΔT is the superheat value. As thermal conductivity of the solid is few order of magnitudes higher than the liquid, the solid can be considered as a lumped model with a uniform temperature, T_s, as shown by Ranjan et al.[40] As ΔT is an input parameter in this model, the only unknown to determine the mass flux is T_{lv}. The energy conservation at the liquid-vapor interface is written as

$$\dot{q}_l = k_l(T_s - T_{lv})\left(\frac{sin\alpha}{r-y} - \frac{cos\alpha}{H+z(y)}\right) \tag{5}$$

$$= \dot{m}h_{fg} + \frac{1}{2}\dot{m}^3\left(\frac{1}{\rho_v^2} - \frac{1}{\rho_l^2}\right),$$

where α denotes turning angle at the liquid-vapor interface and is determined through the profile of the meniscus, dz/dy = $tan\alpha$ at each (y,z) position. The inertia term at the interface $(\frac{1}{2}\dot{m}^3\left(\frac{1}{\rho_v^2} - \frac{1}{\rho_l^2}\right))$ is few order of magnitude smaller than the enthalpy term in the energy conservation and is neglected. The Eqs. 3, 4, and 5 are solved simultaneously by Mathematica to determine the local liquid temperature at the liquid-vapor interface (T_{lv}), local mass flux ($\dot{m}$), and local interfacial heat flux ($\dot{q}_l$). The determined value of $\dot{q}_l$ provides the opportunity to calculate the total interfacial heat flux by the micro/nano structure. The total interfacial heat flux is written as

$$q_t = \frac{\int_{A_{lv}} \dot{q}_l \, dA + h \, A_s(T_s - T_v)}{A_{proj}}, \tag{6}$$

where h denotes the convective coefficient at the solid-vapor interface, and As the area of solid surface exposed for the convective heat transfer, and A_{proj} the total projected area of micro/nano structure. The determined value of h is 38-180 $Wm^{-2}K^{-1}$ in these calculations,[40] depending on the geometry of micro structure. We emphasize that the heat dissipation through thin film evaporation is two orders of magnitude higher than the heat transfer by the natural convection at the solid-vapor interface. In configuration I, the integration of mass flux over the total area of liquid-vapor meniscus is straightforward. In configuration II, the heat flux in the center region between pillars should be calculated separately. For this region, we take the average temperature of T_{lv} between pillars and $\alpha=0$ in Eq. 6 to determine the evaporative heat flux through. In configuration III, in addition to heat flux in the center region, the boundary conditions, r, varies in the area between the vertical wires. That is, the boundary condition to solve Young-Laplace equation varies. We determined r as a function of geometry of the cylindrical pillars and solved the Young- Laplace, Hertz-Knudsen, and energy equations correspondingly to determine the interfacial heat flux in configuration III.
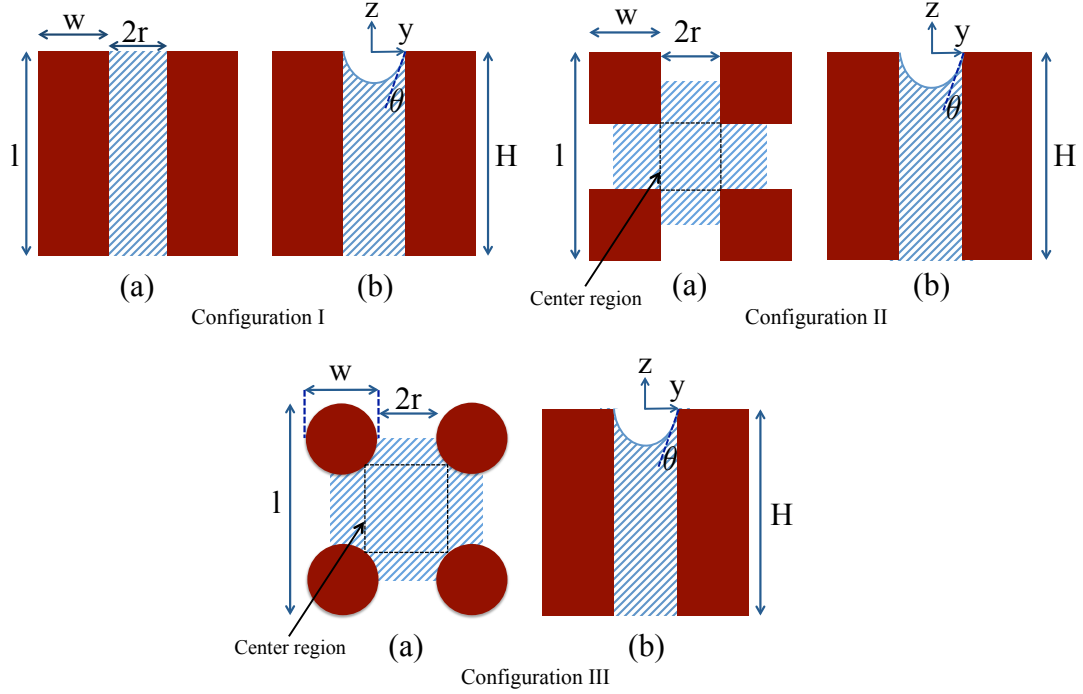
Figure 2. The unit cell of each studied configuration is shown. The top and side views are labeled by (a) and (b), respectively.

2.4. Theoretical Results

In all the theoretical analysis, the working fluid is water, the solid material is copper with temperature of 300.5 K, and the superheat value is 2.5 K, unless otherwise specified. The dimension of simulation box for all the model structures is a square of $2r + w = 100$ μm. Through the discussed approach, we determined the interfacial temperature of liquid along the liquid-vapor interface and the corresponding local mass flux as shown in **Fig. 2**. As shown, the liquid near the three-phase contact line is at higher temperature than the liquid in the centerline. This temperature profile is consistent with the previous studies.[40,44,53,54] Also, the major portion of evaporative mass flux occurs near the three-phase contact line. We determined the interfacial heat flux for all these configurations

through the discussed approach. The interfacial heat flux as a function of width-to-spacing ratio for all three configurations is shown in **Fig. 3**. Note that the small values of interfacial heat flux are caused by the small value of superheat consistent with the previous studies.[40] In the experimental section, high interfacial heat fluxes are achieved by adjusting the superheat.
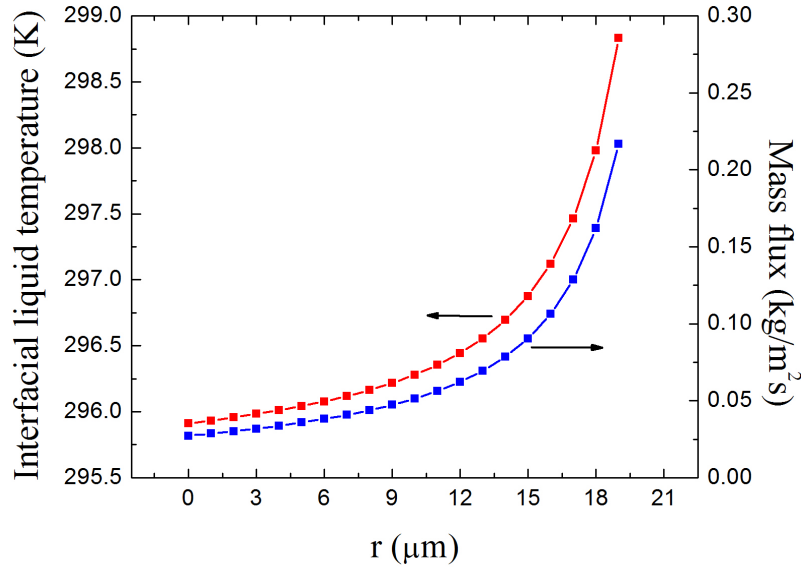

Figure 3. Interfacial liquid temperature and the local mass flux along the meniscus is determined through solution of Young-Laplace, Hertz-Knudsen, and energy equations.

As shown, in configuration I, the interfacial heat flux is a decreasing function of width-to-spacing ratio and reaches a maximum value for the minimum value of width-to-spacing ratio (maximum r). In contrast, both configurations II and III show an optimal value of width-to-spacing ratio to maximize the interfacial heat flux. The optimal value of AR for configurations II and III are 1.27 and 1.5, respectively. Two opposing parameters lead to this optimal aspect ratio: non-uniform evaporative flux across the liquid-vapor interface (i.e. divergent mass flux near the three-phase contact line and negligible mass

11

flux at the centerline) and the total area of liquid-vapor interface for evaporation. For a given area of microstructure (square of $2r + w = 100$ μm), at small width-to-spacing ratio compared to the optimal point (large r between pillars), the total length of three-phase contact line is short resulting into a sharp drop in the evaporative heat flux. In contrast, at higher width-to-spacing ratio compared to the optimal point (small r between pillars), the total area for evaporation decreases resulting into small evaporative heat flux.
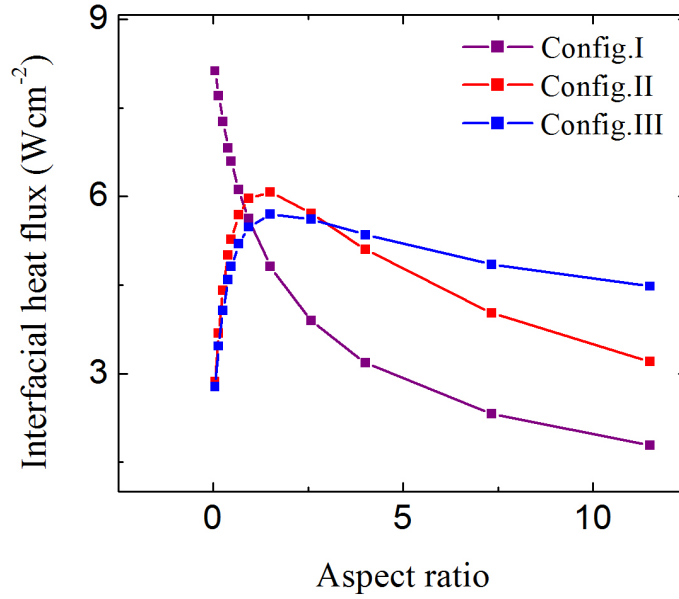

Figure 4. Interfacial heat flux of micro-structures as a function of width-to-spacing ratio for all the three configurations are shown.

We have re-plotted **Fig. 3** as a function of porosity of the micro-structure in **Fig. 11**. To examine the generality of this optimal aspect ratio, the role of other variables on this optimal aspect ratio is studied. We considered configuration II and analyzed the role of pillar height, H, and contact angle, θ on the value of the optimal width-to-spacing ratio. These analyses are shown in **Fig. 4**. The salient point of these figures is the generality of

the optimal width-to-spacing ratio for various contact angles and height of the pillars. This suggests that the optimal width-to-spacing ratio is a general criterion on dimension of micro/nano structures for thin film evaporation. At high values of H, the contribution of normal heat conduction from the solid substrate to the liquid-vapor interface is small. However, at small values of pillar height, this conduction plays a small role in the interfacial heat flux and can slightly change the optimal AR. Furthermore, lower contact angle boosts the interfacial heat flux.

The above analysis provides a general strategy for optimal dimension of micro/nano structures for thin film evaporation. In the next part, we focus on the micro-structures with the optimal width-to-spacing ratio and study the role of density of the pillars per unit area on the interfacial heat flux (i.e. role of dimension of the pillars). The results of this analysis are shown in **Fig. 5**. This figure suggests that the interfacial heat flux is directly proportional to the density of pillars in the micro/nano structures; as the density of pillars increases, the interfacial heat flux increases. That is, smaller size pillars enhance interfacial heat flux. For a given area of micro-structure and at the optimal width-to-spacing ratio, smaller size pillars enhance the total length of three-phase contact line in the micro-structure leading to a rise in the evaporative mass flux. Also, configuration I at small width-to-spacing ratio performs superior to the other model structures. As the dimension of spacing between pillars becomes comparable to thin-film evaporation region, the evaporation rate may reach to a threshold value. We should emphasize that at small-length scale (≤1-2 nm), the length scale can affect the thermo physical properties

(e.g, saturation pressure, density,[80] heat capacity, and thermal conductivity) and the

Fourier equation of heat flux and subsequently the above analysis may break.
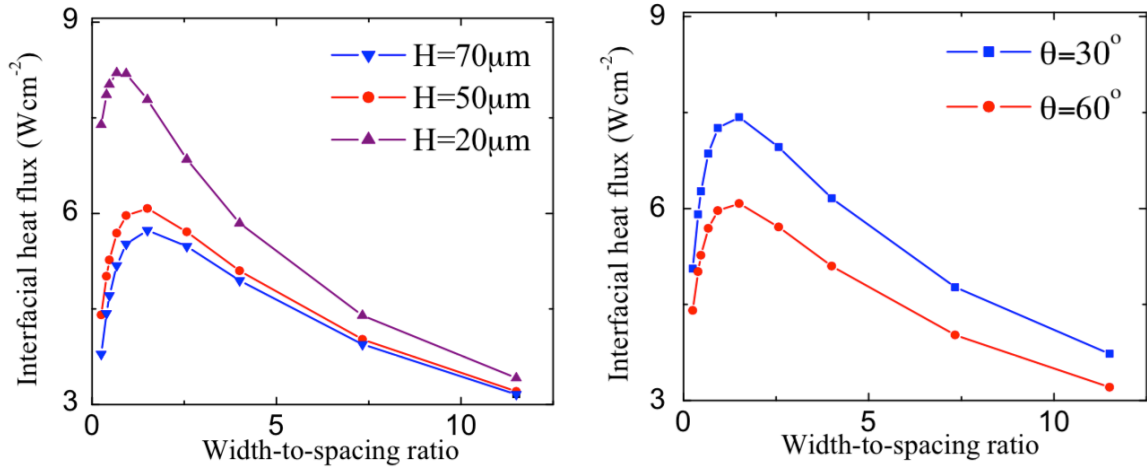

Figure 5. (a) The role of height of pillars on the optimal width-to-spacing ratio for configuration II is shown. (b) The role of contact angle on the optimal width-to-spacing ratio of micro-nano structures is shown.
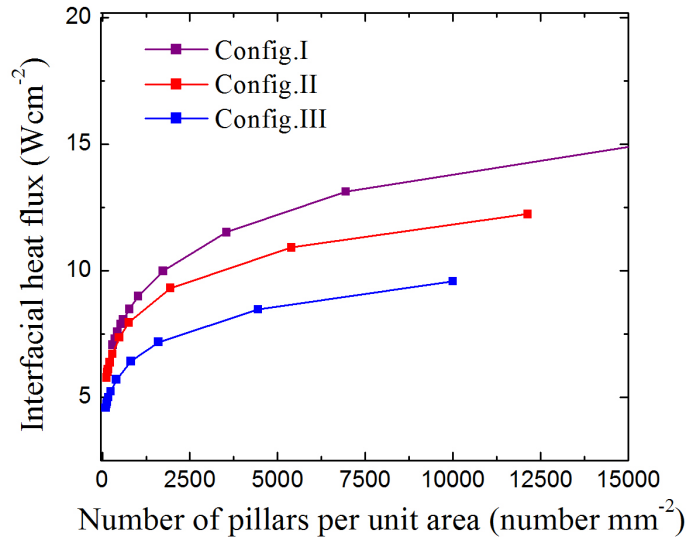

Figure 6. At the optimal width-to-spacing ratio, the role of density of pillars on the interfacial heat flux is shown.

3. Experimental Studies

3.1 Development of Micro-Structures

Once we found the optimal dimension of micro/nano structures for thin film evaporation, we experimentally examined these predictions. We developed a range of micro-structures through micro-fabrication process and we examined their performance for thin-film evaporation. In this work, we developed a range of samples to examine the predictions of the developed theoretical model. For development of micro-structures, 2" Si wafers were obtained from NOVA Electronic Materials; the photolithography masks were developed by Outputcity; the AZ1512 and AZ300 developer were purchased from Integrated Micro Materials; Chromium was purchased from R. D. Mathis Company and Chromium etchant was purchased from Sigma Aldrich. As we need to fabricate deep micro-structures, the conventional micro-fabrication process needs to be modified. Initially, the Si wafer is coated with a thin layer of Cr with thickness of 100-150 nm through e-beam evaporation. On top of this Cr nano-film, a layer of photoresist material, AZ1512 was coated through spin coating method. The thickness of photoresist layer measured by the profilometer is 1.4 ± 0.1 μm. ABM mask aligner in contact mode was used to pattern the photoresist. The time for development of the mask was 50 s. After, we transferred the pattern to the Cr film. We used ion mill for 10-15 mins to pattern the Cr film. The parameters of the ion mils were optimized to only remove the Cr film and not Si substrate. The remaining photoresist material was removed by Acetone and Plasma cleaning. As we need to develop deep micro-structures (depth of 30μm), we used Bosch process for the etching. Once the micro-structure is developed, we removed the extra Cr material from the surface

of the pillars using Cr etchant. The developed micro-structures are divided into two groups and are shown in **Figs. 6 and 7**.

The micro-structures in **Fig. 6** are developed to examine the predictions of optimal aspect ratio at the constant value of 2r + w=100μm, while the micro-structures in **Fig. 7** are fabricated to examine the role of density of pillars on the interfacial heat flux.
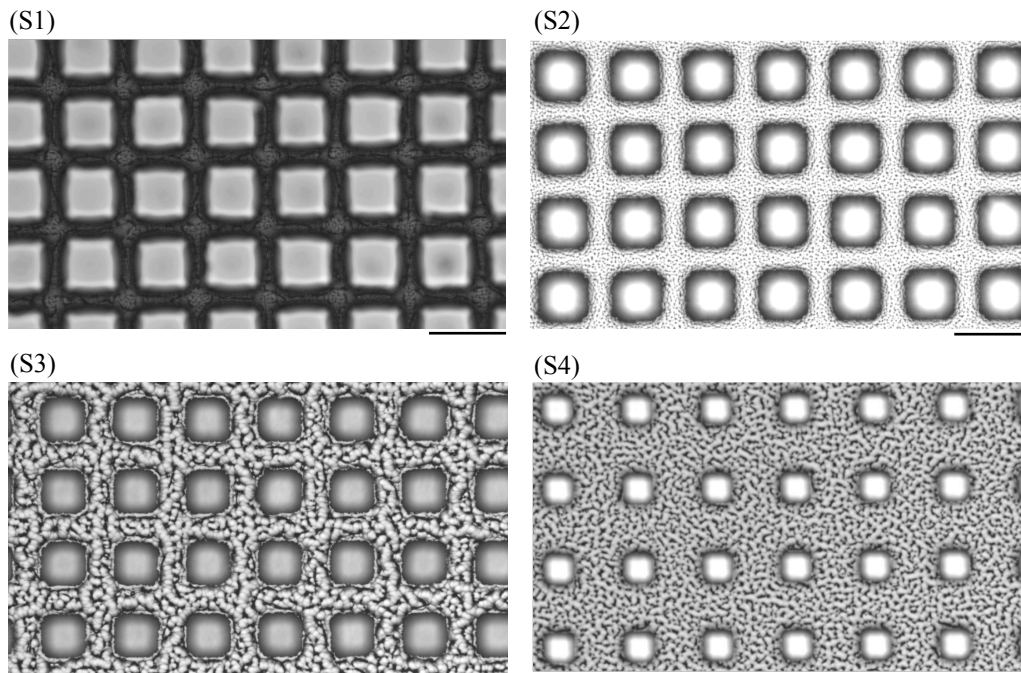

Figure 7. The developed Si micro-structures with various width-to-spacing ratios, but same density of pillars (100 pillars per mm^{-2}) are shown.

3.2. Experimental Procedure and Results

An experimental setup is developed to assess performance of these micro-structures in heat dissipation. The experimental setup is shown in **Fig. 14**. In these experiments, we used Isopropyl alcohol (IPA) as the working fluid to increase the wettability of the structures by the working fluid. The measured contact angle of IPA on the flat Si substrate (with no micro/nano structuring) is 25o±1o. Note that this measured angle represents the angle of meniscus between the pillars in the micro-structure, θ. The experimental setup provides the opportunity to measure the interfacial heat flux by each of the micro-structures in a steady- state condition. At a steady-state condition, the fluid dispensing rate will be equal to the evaporation flux. The heater size placed underneath of the micro-structured surface has 2 cm diameter. The micro- structures in steady-state evaporation condition (corresponding to **Fig. 6**) are shown in **Fig. 8a**. Note that these micro-structures are intended to examine the prediction of optimal aspect ratio. In the steady-sate condition, the wetted area of the fluid evaporation is fixed and does not change with time. We ran each experiment for more than 30 mins and the change in area for each case is less than 1%. The superheat in these experiment kept constant at 15± 0.5 ‰. The evaporative flux by these microstructures includes (1) the thin-film evaporation in the microstructure and (2) the evaporation of free-surface fluid in the inner region. We measured the area of each region by analyzing the experimental pictures with ImageJ software. To compare performance of these micro-structures for thin film evaporation, we need to determine the interfacial heat flux in region (1). To do so, the evaporative heat flux in region (2) is subtracted from the total heat flux. The evaporative heat flux in

17

region (2) is determined through measurement of evaporation of the working fluid on a flat Si substrate.

The developed theoretical model is used to predict the inter- facial heat flux of the micro-structures shown in **Fig. 6**. The inputs to the model are the superheat, contact angle of the working fluid on the structure, and the height of pillars. The predicted and measured interfacial heat flux are shown in **Fig. 8b**. As predicted, there is an optimal ratio in dimensions of micro-structures that maximizes the interfacial heat flux. This agreement between experimental and theoretical results confirms the predictions in the previous section.
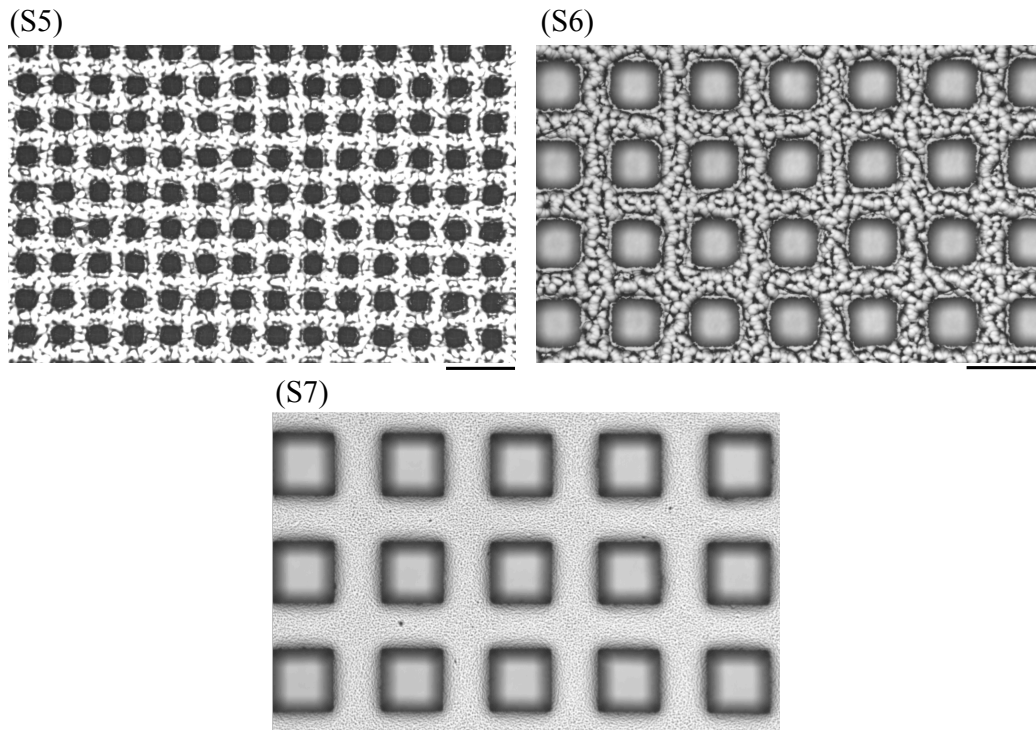

Figure 8. The developed Si micro-structures with the same width-to-spacing ratio, but different density of pillars is shown.
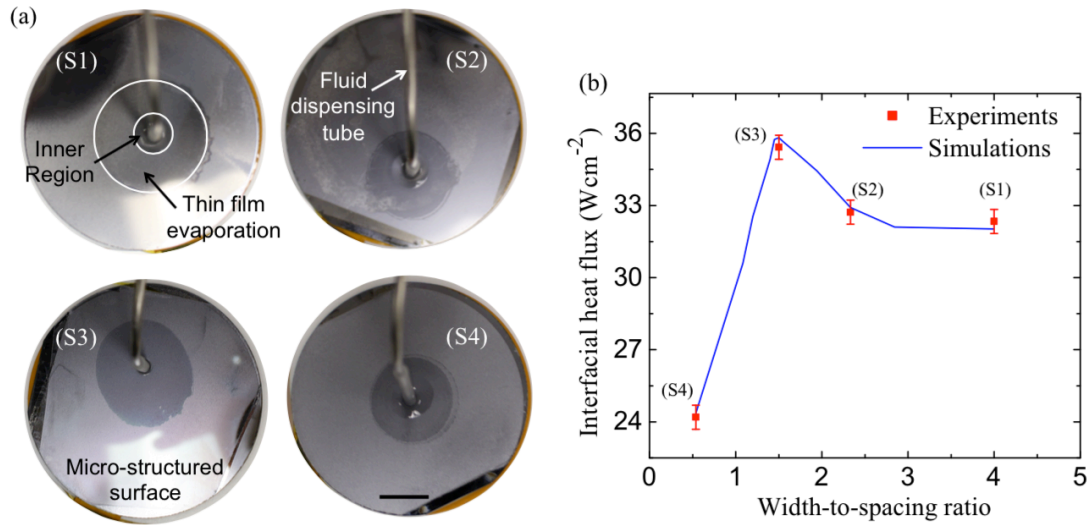
Figure 9. (a) The top view of steady-state evaporation experiments on the micro-structures, shown in **Fig. 7**, are presented. (b) The interfacial heat flux by these structures are predicted with the discussed model above and are compared with the experimental measurements.

In the next step, we examine the role of density of pillars on the interfacial heat flux. The evaporation experiments are similar to the one presented above. The studied microstructures are those shown in **Fig. 7**. The experimental samples for this set of experiments are shown in **Fig. 9a**. We compared the performance of these samples with the prediction as shown in **Fig. 9b**. We emphasize that the inputs to the predictions are only superheat, contact angle, and the height of pillars. The agreement between the measurements and the theoretical predictions confirms that the higher density of pillars in the micro/nano structures boost the interfacial heat flux. Higher density of pillars boosts the three-phase contact line in the micro/nano structure resulting to higher interfacial heat flux.
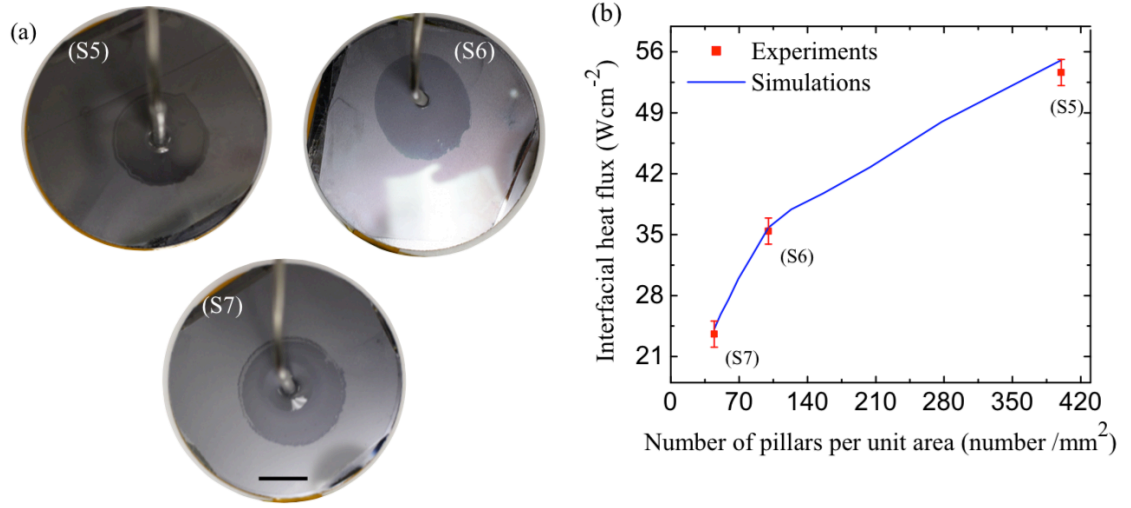
Figure 10. (a) The top view of steady-state evaporation experiments on the micro-structures, shown in **Fig. 8**, are presented. (b) The interfacial heat fluxes by these micro-structures are predicted with the discussed model above and are compared with the experimental measurements.

4. Conclusions

In summary, through theoretical and experimental studies, we show a rational strategy for development of micro/nano structures for thin film evaporation. The opposing roles of non-uniform evaporative heat flux along the liquid-vapor interface and the total area for evaporation leads to an optimal criteria on the dimension of micro/nano structures to maximize the interfacial heat flux. For micro/nano structures with square vertical pillars, the optimal ratio of pillars dimension to the pitch between the pillars is 1.27, and for vertical wires (e.g. nanowires), this ratio is 1.5. At these optimal ratios, as the dimension of pillars decreases (i.e. density of pillars per unit area increases), the interfacial heat flux increases. This optimal ratio is a general criteria and independent of the pillars height, contact angle, and superheat. This work provides a rational direction for micro/nano structuring for thin- film evaporation and provides a platform to develop high-performance thermal management systems to address the future technological demands.

References

(1)   Cho, J.; Goodson, K. E. Thermal transport: Cool electronics. *Nat. Mater*. 2015, 14, 136–137.

(2)   Pop, E. Energy Dissipation and Transport in Nanoscale Devices. *Nano Res*. 2010, 3, 147–169.

(3)   Browne, E. A.; Jensen, M. K.; Peles, Y. Microjet array flow boiling with R134a and the effect of dissolved nitrogen. *Int. J. Heat Mass Transfer* 2012, 55, 825–833.

(4)   Horacek, B.; Kiger, K. T.; Kim, J. Single nozzle spray cooling heat transfer mechanisms. *Int. J. Heat Mass Transfer* 2005, 48, 1425–1438.

(5)   Kandlikar, S. G.; Bapat, A. V. Evaluation of Jet Impingement, Spray and Microchannel Chip Cooling Options for High Heat Flux Removal. *Heat Trans. Eng*. 2007, 28, 911– 923.

(6) Zhang, T.; Peles, Y.; Wen, J. T.; Tong, T.; Chang, J. Y.; Prasher, R.; Jensen, M. K. Analysis and active control of pressure-drop flow instabilities in boiling microchannel systems. *Int. J. Heat Mass Transfer* 2010, 53, 2347–2360.

(7) Fazeli, A.; Mortazavi, M.; Moghaddam, S. Hierarchical biphilic micro/nanostructures for a new generation phase-change heat sink. *Appl.Therm*. Eng. 2015, 78, 380–386.

(8) Kalani, A.; Kandlikar, S. G. Combining liquid inertia with pressure recovery from bubble expansion for enhanced flow boiling. *Appl. Phys. Lett*. 2015, 107, 181601.

(9) Wayner, P.; Kao, Y.; LaCroix, L. The interline heat-transfer coefficient of an evaporating wetting film. *Int. J. Heat Mass Transfer* 1976, 19, 487–492.

(10) Wang, H.; Garimella, S. V.; Murthy, J. Y. An analytical solution for the total heat transfer in the thin-film region of an evaporating meniscus. *Int. J. Heat Mass Transfer* 2008, 51, 6317–6322.

(11) Ranjan, R.; Murthy, J. Y.; Garimella, S. V. Analysis of the Wicking and Thin-Film Evaporation Characteristics of Microstructures. *Journal of Heat Transfer* 2009, 131, 101001.

(12) Jiao, A. J.; Ma, H. B.; Critser, J. K. Evaporation heat transfer characteristics of a grooved heat pipe with micro-trapezoidal grooves. *Int. J. Heat Mass Transfer* 2007, 50, 2905–2911.

(13) Narayanan, S.; Fedorov, A. G.; Joshi, Y. K. On-chip thermal management of hotspots using a perspiration nanopatch. *J. Micromech. Microeng.* 2010, 20, 075010.

(14) Plawsky, J. L.; Fedorov, A. G.; Garimella, S. V.; Ma, H. B. Nano- and Microstructures for Thin-Film Evaporation A Review. *Nanosc. Microsc. Thermophys. Eng.* 2014, 18, 251–269.

(15) Yan, C.; Ma, H. B. Analytical Solutions of Heat Transfer and Film Thickness in Thin- Film Evaporation. *J. Heat Transfer* 2013, 135, 031501.

(16) Su, F.; Ma, H.; Han, X.; Chen, H.-H.; Tian, B. Ultra-high cooling rate utilizing thin film evaporation. *Appl. Phys. Lett.* 2012, 101, 113702.

(17) Ma, H. B.; Cheng, P.; Borgmeyer, B.; Wang, Y. X. Fluid flow and heat transfer in the evaporating thin film region. *Microfluid. Nanofluid.* 2008, 4, 237–243.

(18) Narayanan, S.; Fedorov, A. G.; Joshi, Y. K. Interfacial transport of evaporating water confined in nanopores. *Langmuir* 2011, 27, 10666–10676.

(19) Bar-Cohen, A.; Sherwood, G.; Hodes, M. Gas-assisted evaporative cooling of high den- sity electronic modules. Proceedings of 4th Intersociety Conference on Thermal Phenomena in Electronic Systems (I-THERM). Washington, DC, 1994; pp 32–40.

(20) Dhavaleswarapu, H. K.; Garimella1, S. V.; Murthy, J. Y.; Garimella, S. V. Microscale Temperature Measurements Near the Triple Line of an Evaporating Thin Liquid Film. *J. Heat Transfer* 2009, 131, 061501.

(21) Migliaccio, C. P.; Dhavaleswarapu, H. K.; Garimella, S. V. Temperature measurements near the contact line of an evaporating meniscus V-groove. *Int. J. Heat Mass Transfer* 2011, 54, 1520–1526.

(22) Fernandes, H. C. M.; Vainstein, M. H.; Brito, C. Modeling of Droplet Evaporation on Superhydrophobic Surfaces. *Langmuir* 2015, 31, 7652–7659.

(23) Lu, Z.; Narayanan, S.; Wang, E. N. Modeling of Evaporation from Nanopores with Nonequilibrium and Nonlocal Effects. *Langmuir* 2015, 31, 9817–9824.

(24) Argade, R.; Ghosh, S.; De, S.; DasGupta, S. Experimental investigation of evaporation and condensation in the contact line region of a thin liquid film experiencing small thermal perturbations. *Langmuir* 2007, 23, 1234–1241.

(25) Yiapanis, G.; Christofferson, A. J.; Plazzer, M.; Weir, M. P.; Prime, E. L.; Qiao, G. G.; Solomon, D. H.; Yarovsky, I. Molecular mechanism of stabilization of thin films for improved water evaporation protection. *Langmuir* 2013, 29, 14451–14459.

(26) Wilhelmsen, O.; Trinh, T. T.; Kjelstrup, S.; Bedeaux, D. Influence of curvature on the transfer coefficients for evaporation and condensation of Lennard-Jones fluid from square-gradient theory and nonequilibrium molecular dynamics. *J. Phys. Chem.* C 2015, 119, 8160–8173.

(27) Li, J.; Li, W.; Fang, H.; Zhang, J. Dynamics of Evaporation from Confined Water in an SWCNT in the Presence of an External Field. *J. Phys. Chem.* C 2016, 120, 6493–6501.

(28) Duffey, K. C.; Shih, O.; Wong, N. L.; Drisdell, W. S.; Saykally, R. J.; Cohen, R. C. Evaporation kinetics of aqueous acetic acid droplets: effects of soluble organic aerosol components on the mechanism of water evaporation. *Phys. Chem. Chem. Phys*. 2013, 15, 11634–9.

(29) Souli E, V.; Karpitschka, S.; Lequien, F.; Pren e, P.; Zemb, T.; Moehwald, H.; Riegler, H. The evaporation behavior of sessile droplets from aqueous saline solutions. *Phys. Chem. Chem. Phys.* 2015, 17, 22296–22303.

(30) Brovchenko, I.; Oleinikova, A. Effect of pore size on the condensation/evaporation transition of confined water in equilibrium with saturated bulk water. *J. Phys. Chem.* B 2011, 115, 9990–10000.

(31) Sharma, S.; Debenedetti, P. G. Free energy barriers to evaporation of water in hydrophobic confinement. *J. Phys. Chem. B* 2012, 116, 13282–13289.

(32) Szab o, N.; Totzke, C.; Tributsch, H. Total internal reflectance-infrared structural studies on tensile water formation during evaporation from nanopores. *J. Phys. Chem. C* 2008, 112, 6313–6318.

(33) Sajadi, S. M.; Farokhnia, N.; Irajizad, P.; Hasnain, M.; Ghasemi, H. Flexible artificially networked structure for ambient/high pressure solar steam generation. *J. Mater. Chem. A* 2016, 4, 4700–4705.

(34) Ge, Z.; Cahill, D.; Braun, P. Thermal Conductance of Hydrophilic and Hydrophobic Interfaces. *Phys. Rev. Lett.* 2006, 96, 186101.

(35) Huxtable, S. T.; Cahill, D. G.; Shenogina, S.; Xue, L.; Ozisik, R.; Barone, P.; Usrey, M.; Strano, M. S.; Siddons, G.; Shim, M. et al. Interfacial heat flow in carbon nanotube suspensions. *Nat. Mater.* 2003, 2, 731–734.

(36) Shenogina, N.; Godawat, R.; Keblinski, P.; Garde, S. How wetting and adhesion affect thermal conductance of a range of hydrophobic to hydrophilic aqueous interfaces. *Phys. Rev. Lett.* 2009, 102, 1–4.

(37) Park, J.; Huang, J.; Wang, W.; Murphy, C. J.; Cahill, D. G. Heat transport between Au nanorods, surrounding liquids, and solid supports. *J. Phys. Chem. C* 2012, 116, 26335–26341.

25

(38) Alexeev, D.; Chen, J.; Walther, J. H.; Giapis, K. P.; Angelikopoulos, P.; Koumoutsakos, P. Kapitza Resistance between Few-Layer Graphene and Water: Liquid Layering Effects. *Nano Lett*. 2015, 15, 5744–5749.

(40) Kuang, S.; Gezelter, J. D. Simulating interfacial thermal conductance at metal-solvent interfaces: The role of chemical capping agents. *J. Phys. Chem. C* 2011, 115, 22475– 22483.

(41) Stocker, K. M.; Gezelter, J. D. Simulations of heat conduction at thiolate-capped gold surfaces: The role of chain length and solvent penetration. *J. Phys. Chem. C* 2013, 117, 7605– 7612.

(42) Chen, X.; Mahadevan, L.; Driks, A.; Sahin, O. Bacillus spores as building blocks for stimuli-responsive materials and nanogenerators. *Nat. Nanotech*. 2014, 9, 137–141.

(43) Debuisson, D.; Merlen, A.; Senez, V.; Arscott, S. StickJump (SJ) Evaporation of Strongly Pinned Nanoliter Volume Sessile Water Droplets on Quick Drying, Micropat- terned Surfaces. *Langmuir* 2016, 2679–2686.

(44) Singh, R.; Tundee, S.; Akbarzadeh, A. Electric power generation from solar pond using combined thermosyphon and thermoelectric modules. *Solar Energy* 2011, 85, 371–378.

(45) Xiao, R.; Enright, R.; Wang, E. N. Prediction and optimization of liquid propagation in micropillar arrays. *Langmuir* 2010, 26, 15070–15075.

(46) Srivastava, N.; Din, C.; Judson, A.; MacDonald, N. C.; Meinhart, C. D. A unified scaling model for flow through a lattice of microfabricated posts. *Lab on a chip* 2010, 10, 1148–1152.

(47) Xiao, R.; Wang, E. N. Microscale liquid dynamics and the effect on macroscale propa- gation in pillar arrays. *Langmuir* 2011, 27, 10360–10364.

(48) Ding, C.; Soni, G.; Bozorgi, P.; Piorek, B. D.; Meinhart, C. D.; MacDonald, N. C. A flat heat pipe architecture based on nanostructured titania. *J. Microelectromechanical Sys*. 2010, 19, 878–884.

(49) Nam, Y.; Sharratt, S.; Cha, G.; Ju, Y. S. Characterization and Modeling of the Heat Transfer Performance of Nanostructured Cu Micropost Wicks. *J. Heat Transfer* 2011, 133, 101502.

(50) Bodla, K. K.; Murthy, J. Y.; Garimella, S. V. Evaporation analysis in sintered wick microstructures. *Int. J. Heat Mass Transfer* 2013, 61, 729–741.

(51) Cai, Q.; Bhunia, A. High heat flux phase change on porous carbon nanotube structures. Int. *J. Heat Mass Transfer* 2012, 55, 5544–5551.

(52) Weibel, J. A.; Garimella, S. V.; Murthy, J. Y.; Altman, D. H. Design of integrated nanostructured wicks for high-performance vapor chambers. *IEEE Trans*. Comp. Pack. Manuf. Tech. 2011, 1, 859–867.

(53) Coso, D.; Srinivasan, V.; Lu, M.-C.; Chang, J.-Y.; Majumdar, A. Enhanced Heat Transfer in Biporous Wicks in the Thin Liquid Film Evaporation and Boiling Regimes. *J. Heat Transfer* 2012, 134, 101501.

(54) Xiao, R.; Maroo, S. C.; Wang, E. N. Negative pressures in nanoporous membranes for thin film evaporation. *Appl. Phys. Lett*. 2013, 102, 7–11.

(55) Wang, J.; Catton, I. Evaporation heat transfer in thin biporous media. *Heat and Mass Trans*. 2001, 37, 275–281.

(56) Byon, C.; Kim, S. J. Capillary performance of bi-porous sintered metal wicks. International *Journal of Heat and Mass Transfer* 2012, 55, 4096–4103.

(57) Dai, X.; Yang, F.; Yang, R.; Lee, Y.-C.; Li, C. Micromembrane-enhanced capillary evaporation. *Int. J. Heat Mass Transfer* 2013, 64, 1101–1108.

(58) Byon, C.; Choi, S.; Kim, S. J. Critical heat flux of bi-porous sintered copper coatings in FC-72. *Int. J. Heat Mass Transfer* 2013, 65, 655–661.

(59) Salakij, S.; Liburdy, J. A.; Pence, D. V.; Apreotesi, M. Modeling in situ vapor extraction during convective boiling in fractal-like branching microchannel networks. *Int. J. Heat Mass Transfer* 2013, 60, 700–712.

(60) Pence, D. The simplicity of fractal-like flow networks for effective heat and mass transport. *Exp. Therm. Flui. Sci.* 2010, 34, 474–486.

(61) Hwang, G.; Fleming, E.; Carne, B.; Sharratt, S.; Nam, Y.; Dussinger, P.; Ju, Y.; Kaviany, M. Multi-artery heat-pipe spreader: Lateral liquid supply. *Int. J. Heat Mass Transfer* 2011, 54, 2334–2340. (62) Hwang, G.; Nam, Y.; Fleming, E.; Dussinger, P.; Ju, Y.; Kaviany, M. Multi-artery heat pipe spreader: Experiment. *Int. J. Heat Mass Transfer* 2010, 53, 2662–2669.

(63) Ranjan, R.; Murthy, J. Y.; Garimella, S. V. A microscale model for thin-film evaporation in capillary wick structures. *Int. J. Heat Mass Transfer* 2011, 54, 169–179.

(64) De Gennes, P.-G.; Brochard-Wyart, F.; Quere, D. Capillarity and Wetting Phenomena; *Springer*, 2004.

(65) Vafaei, S.; Wen, D.; Borca-Tasciuc, T. Nanofluid Surface Wettability Through Asymptotic Contact Angle. *Langmuir* 2011, 27, 2211–2218.

(66) Ghasemi, H.; Ward, C. A. Sessile-Water-Droplet Contact Angle Dependence on Adsorption at the Solid-Liquid Interface. *J. Phys. Chem. C* 2010, 114, 5088–5100.

(67) Ghasemi, H.; Ward, C. A. Energy transport by thermocapillary convection during Sessile-Water-droplet evaporation. *Phys. Rev. Lett.* 2010, 105, 136102.

(68) Hertz, H. Ueber die Verdunstung der Flüssigkeiten, insbesondere des Quecksilbers, im luftleeren Raume. *Ann. Phys.* 1882, 17, 177–193.

(69) Knudsen, M. Die maximale Verdampfungsgeschwindigkeit des Quecksilbers. *Ann. Phys.* 1915, 47, 697–708.

(70) Schrage, R. W. A theoretical study of interphase mass transfer; <u>Columbia university press: New York</u>, 1953.

(71) Zientara, M.; Jakubczyk, D.; Litniewski, M.; Holyst, R. Transport of mass at the nanoscale during evaporation of droplets: The Hertz-Knudsen equation at the nanoscale. *J. Phys. Chem. C* 2013, 117, 1146–1150.

(72) Badam, V. K.; Kumar, V.; Durst, F.; Danov, K. Experimental and theoretical investigations on interfacial temperature jumps during evaporation. Experim. *Therm. Fluid Sci.* 2007, 32, 276–292.

(73) Duan, F.; Badam, V. K.; Durst, F.; Ward, C. A. Thermocapillary transport of energy during water evaporation. *Phys. Rev. E* 2005, 72, 56303.

(74) Knudsen, M. The Kinetic Theory of Gases: Some Modern Aspects; Methuene & Company, 1950.

(75) Holyst, R.; Litniewski, M. Evaporation into vacuum: Mass flux from momentum flux and the Hertz-Knudsen relation revisited. *J. Chem. Phys.* 2009, 130, 074707.

(76) Van P. Carey, Liquid-vapor phase change phenomenon; Taylor & Francis Group, LLC, 2008.

(77) Marek, R.; Straub, J. Analysis of the evaporation coefficient and the condensation coefficient of water. *Int. J. Heat Mass Transfer* 2001, 44, 39–53.

(78) Ward, C. A.; Duan, F. Turbulent transition of thermocapillary flow induced by water evaporation. *Phys. Rev. E* 2004, 69, 56308.

(79) Girard, F.; Antoni, M.; Sefiane, K. Infrared Thermography Investigation of an Evapo- rating Sessile Water Droplet on Heated Substrates. *Langmuir* 2010, 26, 4576–4580.

(80) Bocquet, L.; Charlaix, E. Nanofluidics, from bulk to interfaces. *Chem. Soc. Rev.* 2010, 39, 1073–95.

Appendix

Optimal porosity for thin-film evaporation

The interfacial heat flux for different micro-structures as a function of porosity of the structures are shown in **Fig.11**. The porosity in these structures is defined as the ratio of void volume to the total volume in each model structure.

The height of the developed micro-structures is examined with scanning electron microscopy (SEM) and are shown in **Fig. 12**.

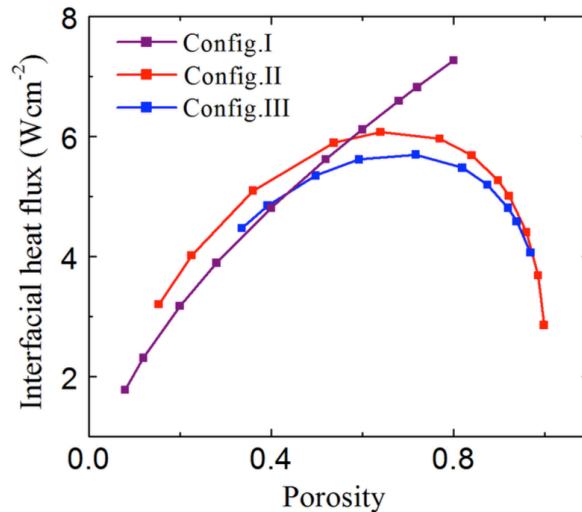**2D heat transfer to the liquid-vapor interface**

Figure 11. The interfacial heat flux in the micro-structures as a function of porosity of the structures is shown. For configuration II and III, there are optimal porosity which maximizes the interfacial heat flux.

The mass flux normal to the liquid-vapor interface is given by the Hertz-Knudsen equation. To determine this mass flux, one needs to determine the normal heat flux to the liquid- vapor interface. The heat transfer to the liquid-vapor interface is two-dimensional; one from the pillars, $\dot{q}_y$, and one from bottom of the micro-structure, $\dot{q}_z$, **Fig. 13**. We

30

calculate the projection of these heat fluxes in the normal direction to the liquid-vapor interface through turning angle, α.

$$\dot{q}_l = \dot{q}_y sin\alpha + \dot{q}_z cos\alpha, \tag{A1}$$

where $tan\alpha = dy/dz$ at each (y,z) coordinate along the liquid-vapor interface. Once we replace the values of $\dot{q}_y$ and $\dot{q}_z$ in the above equation through Fourier equation, one finds

$$\dot{q}_l = k_l(T_s - T_{lv})\left(\frac{sin\alpha}{r - y} - \frac{cos\alpha}{H + z(y)}\right). \tag{A2}$$

We should add that in the Hertz-Knudsen model of evaporation, the accommodation coefficient appears in a multiplier function in the local evaporative mass flux and does not have any dependence on r,
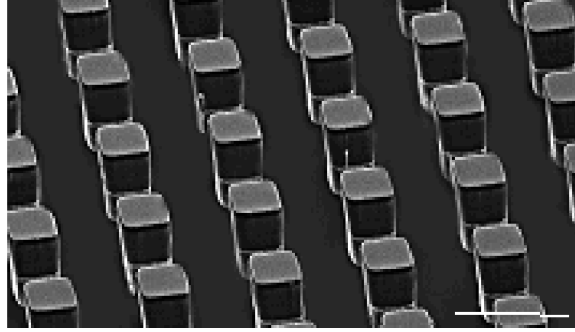
$$\dot{m} \propto \frac{2\sigma}{2 - \sigma}f(r), \tag{A3}$$

Figure 12. The height of the pillars are examined with the Scanning Electron Microscope (SEM) and is approximately 30µm. For this measurement, a sample of micro structures is cut and assembled vertically in the SEM.

where r denotes the radial coordinate between the pillars. Since the optimal width- to-spacing ratio is a direct consequence of f(r) and total area of evaporation, it will be unaffected with different values of accommodation coefficient. We determined the

optimal width-to-spacing ratio for different values of accommodation coefficient and this optimal value is unchanged.

Experimental procedures

The experimental setup includes a fluid dispensing system, which continuously provides fluid to the micro-structure; a controlled flexible heater with diameter of 2 cm attached to the sample and a power system to adjust the temperature of the heater and control superheat. The working fluid in this experimental setup is Isopropyl alcohol (IPA). The microstructure is placed under the fluid dispensing system and simultaneously heated. The fluid from the dispensing system infiltrates to the structures and comes back to the surface by the capillary force for thin film evaporation. The dispensing rate is finely tuned to reach to a steady- state evaporation condition. Each experiment was performed for more than 30 min and the fluctuations in the evaporative mass flux was less than 1%. Once the steady-state condition is achieved, the interfacial heat flux was calculated through fluid dispensing rate, enthalpy of phase change, and the area of thin-film evaporation.
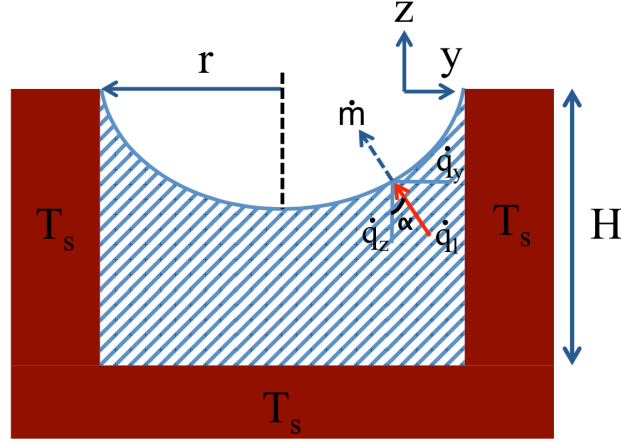
Figure 13. The normal heat flux to the liquid-vapor interface is shown. The normal heat flux comprises of heat flux by the pillars and the heat flux by the bottom substrate.

Error in the measured interfacial heat flux

The interfacial heat flux is measured through energy equation

$$\dot{q}_l = (\dot{m} h_{fg})/A, \tag{A4}$$

where $\dot{m}$ denote the evaporative mass flux in the steady state evaporation, hfg enthalpy of liquid-vapor phase change and A the area of thin film evaporation. The error in the interfacial heat flux $\delta \dot{q}$ is written as

$$\frac{\delta \dot{q}}{\dot{q}} = \frac{\delta \dot{m}}{\dot{m}} + \frac{\delta A}{A}, \tag{A5}$$

where δ denotes the error in the measured values. Note that the error in the values of h_{fg} is so small and negligible. Through the error in the mass injection rate by the syringe pump and the error in the determined surface area of thin film evaporation (ImageJ analysis), we determined the error in the interfacial heat flux.
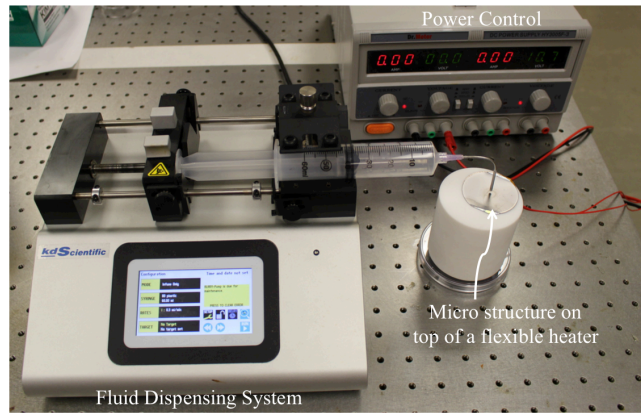
Figure 14. The experimental setup for thin film evaporation studies are shown.